

Chaotic motion of light particles in an unsteady three-dimensional vortex: Experiments and simulation

József Vanyó,^{1,2,*} Miklós Vincze,^{3,4} Imre M. Jánosi,^{3,5} and Tamás Tél^{1,3,6}

¹*Institute of Theoretical Physics, Eötvös Loránd University, Pázmány P. s. 1/A, H-1117 Budapest, Hungary*

²*Department of Physics, Eszterházy Károly College, Eszterházy K. s. 1, H-3300 Eger, Hungary*

³*von Kármán Laboratory for Environmental Flows, Eötvös Loránd University, Pázmány P. s. 1/A, H-1117 Budapest, Hungary*

⁴*Department of Aerodynamics and Fluid Mechanics, Brandenburg University of Technology Cottbus-Senftenberg, Siemens-Halske Ring 14, D-03046 Cottbus, Germany*

⁵*Department of Physics of Complex Systems, Eötvös Loránd University, Pázmány P. s. 1/A, H-1117 Budapest, Hungary*

⁶*MTA-ELTE Theoretical Physics Research Group, Pázmány P. s. 1/A, H-1117 Budapest, Hungary*

(Received 22 October 2013; published 8 July 2014)

We study the chaotic motion of a small rigid sphere, lighter than the fluid in a three-dimensional vortex of finite height. Based on the results of Eulerian and Lagrangian measurements, a sequence of models is set up. The time-independent model is a generalization of the Burgers vortex. In this case, there are two types of attractors for the particle: a fixed point on the vortex axis and a limit cycle around the vortex axis. Time dependence might combine these regular attractors into a single chaotic attractor, however its robustness is much weaker than what the experiments suggest. To construct an aperiodically time-dependent advection dynamics in a simple way, Gaussian noise is added to the particle velocity in the numerical simulation. With an appropriate choice of the noise properties, mimicking the effect of local turbulence, a reasonable agreement with the experimentally observed particle statistics is found.

DOI: [10.1103/PhysRevE.90.013002](https://doi.org/10.1103/PhysRevE.90.013002)

PACS number(s): 47.32.C–, 47.32.Ef, 74.40.De

I. INTRODUCTION

In the past decade, there has been a growing interest in the advection of finite-size inertial particles (for reviews, see [1–5]). However, the active theoretical investigations do not always occur in conjunction with those in laboratories. In particular, very little is known on the experimental side of the dynamics of rigid, spherical buoyant particles, also called bubbles (i.e., particles of smaller density than the fluid).

The behavior of such particles is fundamentally different from the behavior of heavy particles because they have the appealing feature of being pulled toward vortex centers rather than being pushed away. This is due to the change of sign of the centrifugal force with the density difference between the particle and the ambient fluid. Earlier experimental studies concentrated mainly on gas bubbles (of the size of a few microns) in acoustic waves, as illustrated by the recent works of Lohse and co-workers (see, e.g., [6,7]). Our investigations are an extension of such studies in that we examine rigid particles of a much larger size (on the order of millimeters) in a three-dimensional (3D) vortical flow. Another noteworthy feature is the fact that our “bubbles” deviate considerably from the fluid’s motion, and therefore the drag force cannot be considered to be Stokesian. At the same time, the vortical flow exhibits complex features since small-scale turbulence is present.

Cylindrical containers (laboratory glass beakers) with magnetic stirrer bars are generally used as chemical reactors. In a few applications, knowledge of the flow field is also important, in addition to the mixing property of the system [8]. The character of the flow field can serve as an explanation

for some spatial anomalies of the chemical reaction rates in reactors [9], as well as for the chiral selection process in chiral reactions [10]. The flow field and mixing properties around magnetic stirrers can be important in reactor miniaturization [11], and they are also relevant in the study of the extraction efficiency of the stirrer [12]. Knowledge of the flow field is also useful when the aim is that the reacting components should avoid the region of the stirrers [13].

Time-averaged behavior of the flow field generated by magnetic stirrers was studied experimentally in [8], and a Burgers vortexlike flow has been identified (similar to bathtub vortices [14]). The core of the flow is able to keep a buoyant particle, moving up and down, near the axis. Visual observations of [8] also suggest that the particle dynamics appears to be the experimental realization of a motion on a chaotic attractor (projected on the three-dimensional coordinate space of the liquid, of course). The experiment in [8] served as an inspiration for our present work. The goals of the present paper are to improve the model of the flow field and to understand the motion of a buoyant particle in detail. We will achieve these goals through a combination of experiments and computer simulations.

Specific features of our problem are that (i) due to a strong downwelling, buoyant particles remain localized in a finite vertical region (while exhibiting irregular motion) for a long time; (ii) the typical particle Reynolds number is much larger than unity, hence a more general force than Stokesian drag should be taken into account; (iii) in addition to a large-scale vortical structure, the effect of small-scale turbulence turns out to be relevant; and (iv) turbulence proves to be not homogeneous, therefore a nontrivial height dependence should be taken into account.

Preliminary experimental runs have been performed in which several identical particles were released simultaneously from a small, compact initial domain at the water surface.

*vanyoj@general.elte.hu

The trajectories of initially adjacent particles visibly tended to diverge from each other after a few seconds, though they remained confined to the aforementioned vertical region. This qualitative observation—the apparent sensitivity of the system to initial conditions—can be considered to be a suggestion of the chaotic nature of the particle motion. However, since the applied image-processing-based particle-tracking algorithm would not have been able to differentiate between particles and track their trajectories separately, no direct qualitative measure of chaoticity (e.g., a Lyapunov exponent) could be determined experimentally. For the same reason, all the experimental data presented here are results of single-particle measurements. Such technical measurement limitations were among the main reasons that triggered the numerical part of this work, aiming to better understand the dynamics of inertial particles in a vortex flow.

The paper is organized as follows. A summary of the experimental results is given in Sec. II. The construction of a periodically time-dependent model flow, and the equation of motion for the particle, are presented in Sec. III. Section IV is devoted to an analysis of the advection dynamics and a description of the attractors. We show that the regular attractors of the time-independent case might combine into a single chaotic attractor in the presence of a periodic driving. The existence of chaos in the parameter space is, however, found to be rather limited, and to lie far away from any realistic values. Section V is devoted to modeling the effects of turbulence on the particle via introducing a random force and to presenting the corresponding simulations. Finally, in Sec. VI we discuss the implications of the results. Technical details are relegated to an Appendix.

II. EXPERIMENTAL RESULTS

The experiment consists of a rotating magnetic stirrer generating a vortex in a cylindrical container filled with tap water at room temperature (see the left panel of Fig. 1). In our set of experiments, the radius of the cylinder is $R = 11.2$ cm, the water height is $H_w = 30$ cm, and the length and diameter of the stirrer are $l = 4$ cm and $d = 1$ cm, respectively. The rotational frequencies of the stirrer (f) used in the experiments are given in the first row of Table I. The cylinder is wide enough to ensure that the f dependence of the water height H_w is negligible.

We take a basic result of [8]: the particle image velocimetry (PIV) method revealed that the time-averaged tangential component of the flow can be described by the Burgers form:

$$u_t = \frac{C}{r}(1 - e^{-r^2/c^2}), \quad (1)$$

where the parameter c is the radius of the vortex core, and C is the vortex strength (defined as 2π times the circulation along a circle far from the center). By using this component, simple estimations for the average funnel height (\bar{h}) and for the average half-width (\bar{b}) of the funnel (defined as the radius of the funnel at half of its height) lead to

$$\bar{h} = \ln 2 \frac{C^2}{c^2 g} \quad \text{and} \quad \bar{b} \approx c, \quad (2)$$

where g is the gravitational acceleration.

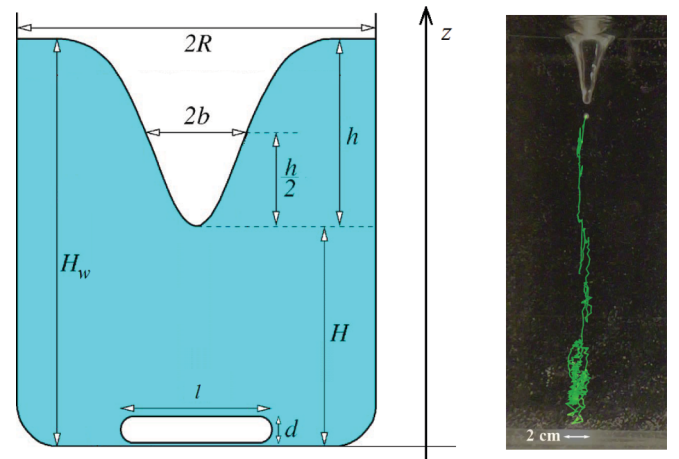


FIG. 1. (Color online) Schematic diagram of the experimental setup (left) and the trajectory of a tracked particle (green line) from an experiment over 25 s (right). The geometrical parameters in the left panel are the radius of the cylinder R , the water height H_w , the height of the funnel h , and the half-width of the funnel b . $H = H_w - h$ is the distance between the deepest point of the funnel and the bottom of the container, and l and d are the length and diameter of the stirrer bar, respectively.

The vortex strength was found to be directly proportional to the frequency f of the stirrer [8]:

$$C = A_0 2\pi f, \quad (3)$$

while the average half-width of the funnel appeared to be independent of frequency f .

Unfortunately, the planar PIV approach is not suitable to study the inner part of the flow. Other methods should, therefore, be used to study the core of the vortex. This is why we carried out new, detailed measurements of the funnel parameters and of the particle dynamics. The latter approach is based on the following observation: A spherical macroscopic buoyant particle (i.e., lighter than water) is put on the surface of the water. After a while, the particle gets to the bottom of the funnel. Theoretically, the particle should remain on the surface because of the buoyancy force, but the fluctuations of the flow field, which lead to a change of the location of the funnel, are able to pull the particle down from the surface if the frequency of the stirrer is large enough. The particle carries out a chaotic-looking motion in the bulk of the water, but after some time it reaches the bottom from where the stirrer kicks it to outer regions of the container, where it rises up to the surface.

TABLE I. Essential features of the funnel versus stirrer frequency f . The rows of the table contain the frequency ω of flow oscillations, the average funnel height (\bar{h}), and the standard deviation of the funnel height [$s(h)$] divided by \bar{h} . The typical magnitude of the errors is 5%.

f (Hz)	5.0	7.5	10.0	12.5	15
ω (Hz)	0.39	0.55	0.91	1.22	1.07
\bar{h} (cm)	1.07	2.30	4.36	7.48	11.01
$s(h)/\bar{h}$	0.12	0.09	0.07	0.07	0.07

Both the funnel and particle properties are monitored by means of video recordings. The right panel of Fig. 1 shows a typical particle trajectory after the detachment from the surface.

In our experiments, the particle is made of low-density polyethylene (LDPE), its density is $\rho_p = 0.85 \text{ g/cm}^3$, and a typical radius is $a = 0.2 \text{ cm}$. The temporal resolution of the recorded movies is $\tau_{\text{sample}} = 1/30 \text{ s}$.

There are several ways to estimate the Reynolds number characterizing the flow. One of its dominant features is a downwelling jet in the vortex axis. The characteristic width of this jet is about $L = 1 \text{ cm}$, as also suggested by the scale given in the right panel of Fig. 1. A typical vertical velocity in the vortex center is found to be $U = 10 \text{ cm/s}$, from which $\text{Re} = UL/\nu = 1000$ follows with the kinematic viscosity $\nu = 0.01 \text{ cm}^2/\text{s}$ of water. Because of the high Reynolds number, small turbulent vortices are expected to be present around the vortex axis.

To estimate the turbulence properties, we carried out a careful analysis of the PIV velocity data at a distance of about 4 cm from the center (where data are already at the edge of becoming reliable). Our analysis revealed that the velocity fluctuations u' are about 15% of the tangential velocity there. Assuming this ratio remains valid even at $L = 1 \text{ cm}$ from the center, we obtain values from Eqs. (1)–(3) for a typical frequency $f = 10 \text{ Hz}$ and $u_t = 52 \text{ cm/s}$, from which $u' \approx 8 \text{ cm/s}$. Since the characteristic scale of the flow is $L = 1 \text{ cm}$, with this u' the energy dissipation rate [15] is $\epsilon = u'^3/L \approx 510 \text{ cm}^2/\text{s}^3$. The Kolmogorov length and temporal scale are found to be $\eta = (\nu^3/\epsilon)^{1/4} \approx 0.007 \text{ cm}$ and $\tau_\eta = (\nu/\epsilon)^{1/2} \approx 0.004 \text{ s}$, respectively. It is worth noting that the Reynolds number $\text{Re}' = u'L/\nu$ based on the integral scale of turbulence turns out to be 800, and it is the same order of magnitude as that of the previous estimate.

A. Funnel properties

Figure 2 displays the height h of the funnel versus time as obtained from a video record. The insets show the power

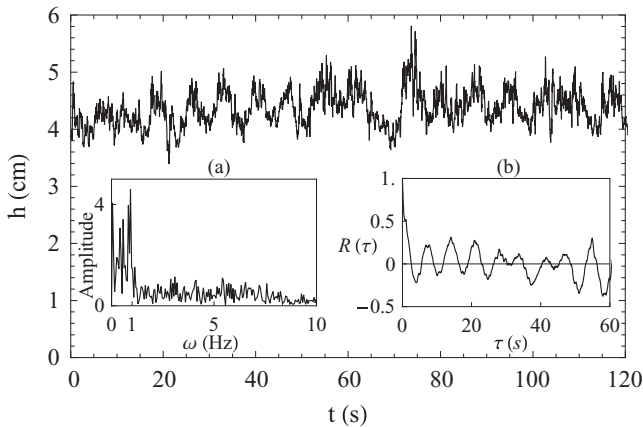


FIG. 2. Height h of the funnel vs time at stirrer frequency $f = 10 \text{ Hz}$. Insets (a) and (b) show the power spectrum and the autocorrelation function, respectively. The period of the latter is $T = (6.9 \pm 0.3) \text{ s}$ and the corresponding frequency is $\omega = (0.91 \pm 0.4) \text{ Hz}$.

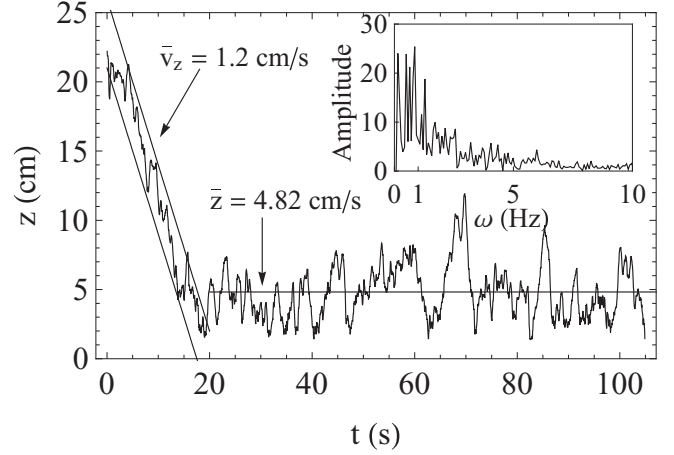


FIG. 3. The vertical coordinate z of the particle vs time. $f = 10 \text{ Hz}$. Inset: power spectrum of $z(t)$. The extracted data are $\bar{v}_z = 1.2 \text{ cm/s}$, $\bar{z} = 4.82 \text{ cm}$.

spectrum and the autocorrelation function of the time series. The large peaks indicate a periodicity in the movement of the funnel. This may be due to an overall periodic time dependence of the flow (which is disturbed by turbulence). The main angular frequency ω of the flow oscillations is found to depend on the stirrer frequency f ; see Table I. According to our experiments, the half-width is $b = 0.75 \pm 0.05 \text{ cm}$ (a mean of 50 measurements), and the coefficient A_0 in (3) is determined from the average funnel heights (\bar{h}) of Table I to be $A_0 = 0.99 \pm 0.08 \text{ cm}^2$.

B. Particle dynamics

Figure 3 exhibits a time series of the vertical coordinate $z(t)$ of a particle. The particle is released from the surface at the bottom of the funnel at zero vertical velocity. In the first period of motion (for $t \lesssim 20 \text{ s}$), it descends to a given mean depth as illustrated in Fig. 3. An average sinking velocity \bar{v}_z characterizes this part. After the particle reaches the lower region (second period, $t \gtrsim 20 \text{ s}$) it dances for a longer time and eventually reaches the bottom (at $t \approx 105 \text{ s}$). Then the particle escapes as it hits the stirrer at about $z = 1 \text{ cm}$ and is kicked out. The average height \bar{z} of the second period is shown by the horizontal line. The frequency $\omega = 0.91 \text{ Hz}$ of flow oscillations is also found to appear in the power spectrum of function $z(t)$.

At the lowest studied stirrer frequency, $f = 5 \text{ Hz}$, the axial flow is not strong enough to keep the particle under the surface,

TABLE II. Statistical properties of the particle dynamics for the different stirrer frequencies f . $s(z)$ and σ_z denote the standard deviation of the dataset z and of the histograms in Fig. 5. The unit of data is cm when not stated otherwise. The last column exhibits the symbols for the different frequencies used throughout the paper.

f (Hz)	\bar{v}_z (cm/s)	\bar{z}	$s(z)$	σ_z	Sym.
7.5	1.1 ± 0.4	5.37	3.35	3.48	●
10.0	1.5 ± 0.3	4.78	2.86	4.60	■
12.5	2.1 ± 0.9	4.83	2.35	4.74	▲

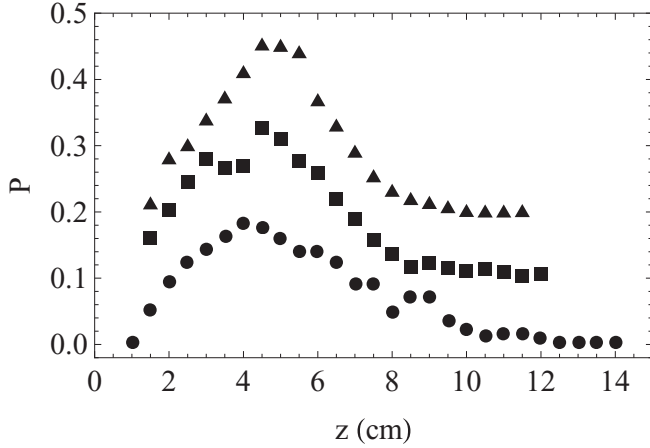


FIG. 4. The height distribution $P(z)$ in the second period of the motion (see Fig. 3). Different symbols mark different stirrer frequencies (see Table II). For better visibility, the upper two graphs are shifted by $\Delta P = 0.1$ each.

while at the highest frequency $f = 15$ Hz the flow is so strong that the particle simply goes through the studied region. We therefore concentrate on the stirrer frequency values $f = 7.5$, 10, and 12.5 Hz. In these cases, it is possible to study the particle motion statistically by using video recordings of an approximate length of 5 min. The results are summarized in Table II. The first column contains the average sinking velocities along with their standard deviations.

The second period of motion can be considered to represent a steady state. We can then determine the probability distribution $P(z)$ of height z . The results are shown in Fig. 4. Visits at larger heights have a relatively low probability. The motion is probabilistic, and—as mentioned in the Introduction—appears to be sensitive to the initial conditions, which can be interpreted as a sign of possible chaoticity of the finite-size particle dynamics. We also study the velocity increments $\Delta \vec{v}$ of the time series as in [16]. Figure 5 shows the histograms of the vertical component of the velocity increments Δv_z between

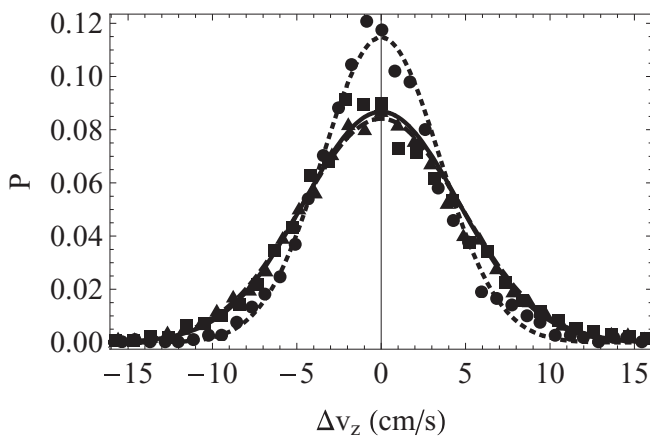


FIG. 5. Histograms of the vertical component of the velocity increments, Δv_z , from the time series. The fitted σ_z 's in (4) can be found in the fourth column of Table II. (The symbols correspond to those in Table II.)

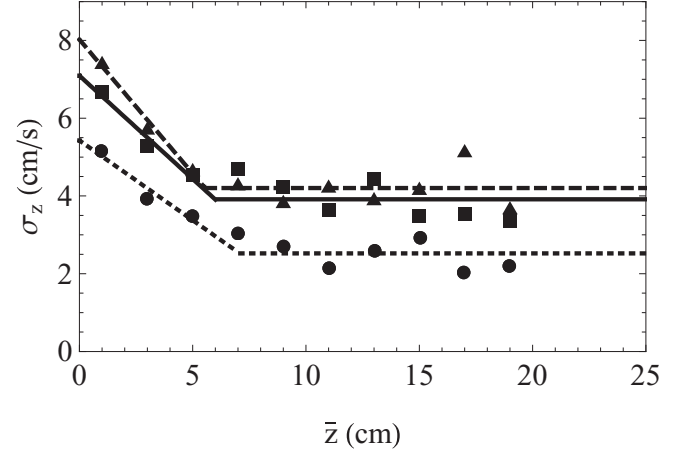


FIG. 6. Dependence of σ_z on the average height \bar{z} . The fitted curves (piecewise linear functions) are of the form of (5) with parameters A , B , and M given in Table III. (The symbols correspond to those in Table II.)

subsequent frames of the video record. The distributions are found to be approximately Gaussian with zero mean and a standard deviation σ_z :

$$P(\Delta v_z) = \frac{1}{\sqrt{2\pi}\sigma_z} \exp\left(-\frac{\Delta v_z^2}{2\sigma_z^2}\right). \quad (4)$$

σ_z can be interpreted as the average of the modulus of the velocity increments. A detailed study of several records indicates that σ_z depends on the average height \bar{z} . The height dependence of the average velocity increment σ_z is exhibited in Fig. 6 and Table III, and it suggests a form

$$\sigma_z(\bar{z}) = \begin{cases} A\bar{z} + B & \text{if } \bar{z} \leq \frac{M-B}{A}, \\ M & \text{if } \bar{z} > \frac{M-B}{A}. \end{cases} \quad (5)$$

The vertical components of the successive velocity increments are clearly anticorrelated. Figure 7 shows the correlation functions for the three given stirrer frequencies (see Table II). The observed one-step anticorrelation might also be considered to be a hint of the existence of small turbulent eddies in the background [17].

Particles do not stay very long in the bulk of the flow. Escape typically happens at the bottom when a particle hits the stirrer and is kicked out. In practice, the lifetimes can be measured by a simple stopwatch. The mean lifetime \bar{T} is measured in 100 experimental runs and found to be in the range of (14 s, 50 s).

TABLE III. Parameters to (5) obtained from a fit to Fig. 6.

f (Hz)	A	B	M
7.5	-0.411	5.43	2.52
10.0	-0.531	7.09	3.92
12.5	-0.689	8.02	4.20

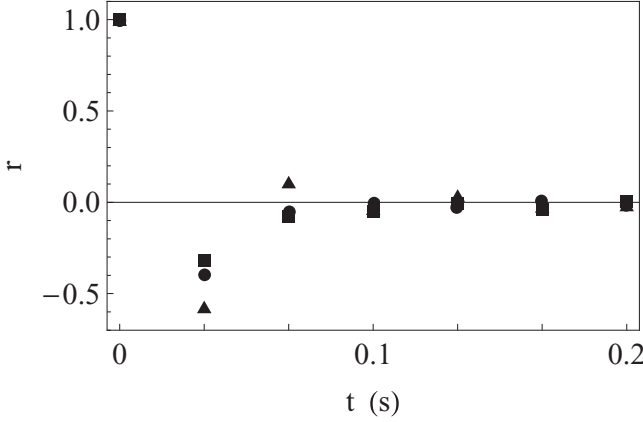


FIG. 7. Correlation functions $r(t)$ of the vertical component of the velocity increments $\Delta v_z(t)$ in all three cases. (The symbols correspond to those in Table II.) At time zero, all three symbols coincide. The measured points are taken at multiples of the sampling time $\tau_{\text{sample}} = 1/30$ s. The velocity components are practically uncorrelated for $t \geq 2\tau_{\text{sample}}$, whereas clear negative correlation can be found at $t = \tau_{\text{sample}}$.

III. MODEL

A. Model flow

An important feature of the vortex governing the flow within the container is its finite height, denoted by H . To construct the simplest model flow, we ignore the effect of a free surface as the well-known Burgers vortex does, and we take, in the notation of Fig. 1, $H_w = H$ ($h = 0$). Because of the cylindrical symmetry of the container, it is natural to use cylindrical coordinates. Axis z is chosen to coincide with the axis of the vortex. The level $z = 0$ ($z = H$) is the bottom (top) of the flow. It is easy to satisfy the top and bottom boundary conditions if the vertical component of the velocity of the model flow is chosen as

$$u_z = -u_{z,\text{max}} f(r)g(z) \quad (6)$$

with $g(0) = 0$ and $g(H) = 0$. Function f determines the velocity profile of the vertical component and has a maximum in the axis ($r = 0$), while function g gives the height dependence. Maxima of f and g are chosen to be 1, so that $u_{z,\text{max}}$ is the maximum value of the vertical velocity component. A simple choice for function g is a polynomial

$$g(z) = 1 - \left| \frac{2z}{H} - 1 \right|^n \quad (7)$$

with n as a positive integer. Exponent n will be fixed later, but $H = 25$ cm will be kept constant throughout the paper.

This form ensures that the maximum of the downwelling velocity occurs at height $z = H/2$. Our choice for f is

$$f(r,t) = I(t) \left[1 - \left(\frac{r}{\mathcal{R}_0} \right)^2 \right] \quad (8)$$

and $f \equiv 0$ for $r > \mathcal{R}_0$, where $\mathcal{R}_0 = 1$ cm. Note that this is a parabolic profile corresponding to a wall at $\mathcal{R}_0 = 1$ cm. This is, of course, an approximate form expressing that considerable downwelling velocities occur in a restricted region only. The use of this form is supported by our observations according to

which the particle concentrates most often to a region $r < 0.5$ cm from the vortex center.

The general form of $I(t)$ is $I(t) = 1 + \Delta I \sin(\omega t)$, where ω is the overall period of the flow oscillations, and ΔI represents the amplitude. A similar time dependence is often used in the literature on inertial particle dynamics (see [18–20]). We estimate the dimensionless ΔI as $\Delta I \approx s(h)/\bar{h}$ (see Table I). For $\Delta I = 0$, the flow is time-independent.

We suppose that the radial component of the flow also factorizes

$$u_r = u_{z,\text{max}} F(r)G(z). \quad (9)$$

Because the fluid is incompressible, the incompressibility condition

$$\frac{1}{r} \frac{\partial(ru_r)}{\partial r} + \frac{1}{r} \frac{\partial u_t}{\partial \varphi} + \frac{\partial u_z}{\partial z} = 0 \quad (10)$$

yields two relations between factors f , g , F , and G :

$$G(z) = g'(z) \quad (11)$$

and

$$f(r) = \frac{F(r)}{r} + F'(r). \quad (12)$$

By taking into account that $u_r = 0$ in the axis ($r = 0$), we find $F(0) = 0$. So one can easily check that F appears as

$$F(r) = \frac{1}{r} \int_0^r r' f(r') dr' = I(t) \left(\frac{r}{2} - \frac{r^3}{4\mathcal{R}_0^2} \right). \quad (13)$$

The third, tangential component of the flow is given by (1) (the Burgers form). Figure 8 provides an overview of the flow field for $n = 2$ in (7) as the simplest nontrivial example. The Appendix presents how the shape of the funnel can be obtained when the effect of the free surface is taken into account. In this case, $H_w > H$ and their difference determines the funnel height \bar{h} .

B. Particle dynamics

The equation of motion of a small spherical particle of radius a in a velocity field $\mathbf{u}(\mathbf{r}, t)$ is

$$m_p \ddot{\mathbf{r}} = m_f \frac{D\mathbf{u}(\mathbf{r}, t)}{Dt} + \frac{1}{2} m_f \left(\frac{D\mathbf{u}(\mathbf{r}, t)}{Dt} - \dot{\mathbf{r}} \right) + (m_p - m_f) \mathbf{g} + \mathbf{F}_{\text{drag}}, \quad (14)$$

where D/Dt is the hydrodynamic derivative taken comoving with the flow. m_p is the mass of the particle and m_f is the mass of the fluid displaced by the particle [21,22]. This equation has been shown to be the valid equation of motion for small particles in several papers (see, e.g., [23–26]).

The key feature is that the drag force, \mathbf{F}_{drag} , depends sensitively on the particle Reynolds number,

$$\text{Re}_p = \frac{2a|\dot{\mathbf{r}} - \mathbf{u}|}{\nu}, \quad (15)$$

and it also contains an integral, the so-called history force [1,21,22,27], being also strongly Re_p -dependent. [It is the $\text{Re}_p \ll 1$ limit of (14) which is called the Maxey-Riley equation [21,22,27].]

In our experiments, we often observe a particle hovering at a given height in the center of the vortex for a while. Since there

is a strong downwelling of speed ≈ 10 cm/s in the center, the relative velocity is then of the same value, and $\text{Re}_p = 0.4 \text{ cm} \times 10 \text{ cm/s} / (10^{-2} \text{ cm}^2/\text{s}) = 400$, thus we conclude that the particle Reynolds number can reach up to 400 at least.

At increasing Reynolds numbers, the relative weight of the history force is decreasing. A qualitative explanation of this fact can be given by observing that the history force (even if it remained Re_p -independent) provides a contribution proportional to the velocity difference and hence to the Stokes drag (see, e.g., [28]), but this term becomes negligible compared to the full nonlinear drag for increasing relative speeds. In our simple model, we therefore neglect the history force (as in other approaches describing particle advection in similar flows [18–20]), but we take the nonlinear drag into account via a semiempirical formula [29,30],

$$\mathbf{F}_{\text{drag}} = -\frac{1}{2}\rho_f C_D(\text{Re}_p) a^2 \pi (\dot{\mathbf{r}} - \mathbf{u}) |\dot{\mathbf{r}} - \mathbf{u}|, \quad (16)$$

where

$$C_D(\text{Re}_p) = \frac{24}{\text{Re}_p} + \frac{6}{1 + \sqrt{\text{Re}_p}} + 0.4, \quad (17)$$

and Re_p [see Eq. (15)] is the particle Reynolds number.

After substituting \mathbf{F}_{drag} in (14), the equation of motion of the particle is

$$\ddot{\mathbf{r}} = \frac{3}{2}R \frac{D\mathbf{u}(\mathbf{r},t)}{Dt} - \frac{3}{8} \frac{R}{a} C_D(\text{Re}_p) (\dot{\mathbf{r}} - \mathbf{u}) |\dot{\mathbf{r}} - \mathbf{u}| + \left(1 - \frac{3}{2}R\right) \mathbf{g}, \quad (18)$$

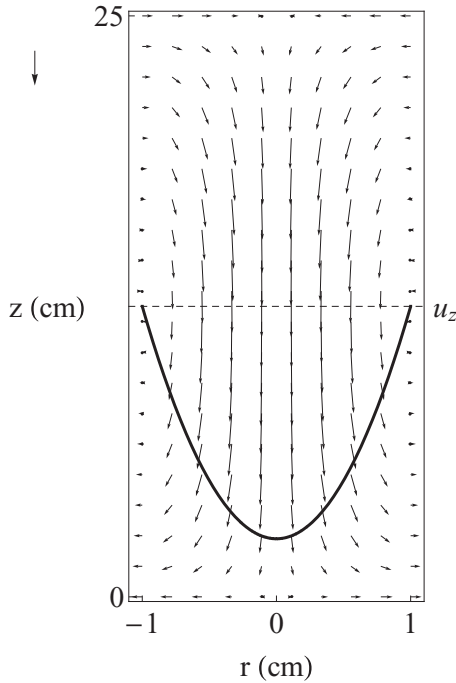


FIG. 8. Vertical section of the time-independent velocity field of the model across the axis of the vortex, represented by arrows. A velocity vector corresponding to 10 cm/s is indicated at the left margin. The continuous line represents the velocity profile of $u_z(r)$ at $z = 12.5$ cm in arbitrary units. The parameters are $n = 2$, $u_{z,\text{max}} = 10$ cm/s, and $f = 10$ Hz.

where

$$R = \frac{2\rho_f}{\rho_p + 2\rho_f} \quad (19)$$

is the density ratio. In the simulations, we take $g = 1000 \text{ cm/s}^2$, $\nu = 0.01 \text{ cm}^2/\text{s}$, $\rho_f = 1 \text{ g/cm}^3$ (water), and the properties of the particle used in the experiments: $a = 0.2 \text{ cm}$ and $\rho_p = 0.85 \text{ g/cm}^3$ ($R \approx 0.74$).

When the particle size becomes comparable to the flow's characteristic scale, the so-called Faxen correction should be added to many of the terms in the equation of motion. The one appearing in the velocity difference is, for example (see [1,21,22,31]), $a^2/6\Delta\mathbf{u}$ (Δ being the Laplacian). The order of magnitude of this term is $(1/6)(a/L)^2 U \approx 0.007U$, which we can neglect in our simple model.

IV. MODEL ANALYSIS

A. Time-independent flow

First we study the time-independent case $\Delta I = 0$. Since n in (7) will be fixed from the data of the time-dependent flow, here we take $n = 2$ as an example. We find two types of particle attractors in the system. Both can be described by constant r and z coordinates, denoted by r^* and z^* . The existence and stability of the fixed points and limit cycles depend strongly on the value of $u_{z,\text{max}}$. These dependencies are shown in Fig. 9. For higher n values, the bifurcation diagram is qualitatively the same but its shape is similar to a parabola of order $1/n$.

The density of the particle is smaller than that of the fluid, so buoyancy and “antacentrifugal” forces act upon the particle. Both of them are independent of $u_{z,\text{max}}$. If $u_{z,\text{max}}$ is small, the downward flow is not strong enough to keep the particle under the water, and no attractors exist. At $u_{z,\text{max}} \approx 10.4$ cm/s, a tangent bifurcation occurs and a stable (solid green line) and an unstable (dashed red line) fixed point appears on the axis, as the upper panel of Fig. 9 indicates. This occurs near $z = H/2$ since, as we saw, downwelling is strongest along the

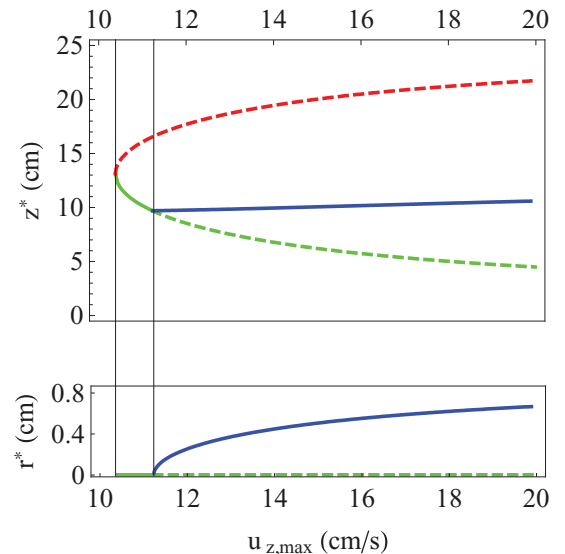


FIG. 9. (Color online) Attractor coordinates r^* , z^* as functions of $u_{z,\text{max}}$ for $f = 10$ Hz and $n = 2$ in the time-independent flow.

axis at $z = H/2$ [see (7)]. The upper (unstable) fixed point is repulsive in the z direction for any $u_{z,\max}$. The radial stability of a fixed point depends on the difference of the anticentrifugal force and the radial component of the drag force. For $10.4 < u_{z,\max} < 11.2$ cm/s, both fixed points are attractive from the radial direction. As $u_{z,\max}$ is increased continuously, u_r and the radial component of the drag force are also increasing. At $u_{z,\max} \approx 11.2$, the difference becomes zero, and the lower fixed point becomes repulsive from the radial direction and loses its stability. This is a saddle-node bifurcation: at the same time another stable state arises that corresponds to a limit cycle around the axis (solid blue line with $r^* > 0$). The limit cycle can be characterized by a constant angular velocity of the particle.

B. Periodically time-dependent flow

To get an overview of the dynamics in the time-periodic case ($\Delta I > 0$), we present in Fig. 10 the plane spanned by the two most important parameters $u_{z,\max}$ and ΔI . Figure 11 shows typical particle trajectories in the r - z plane in different regimes of Fig. 10.

Basically, the parameter space can be divided into two parts. In the first part (regions I and II), the particle can escape, so the motion takes a finite amount of time. In this part, two qualitatively different dynamics exist. In the simpler case, the particle goes only upward and reaches the surface ($z = H$) in a short time (region I), while in the other case transient chaotic motion [32] is possible and the lifetime can be long (region II). In the other part of the parameter space (regions III, IV, and V),

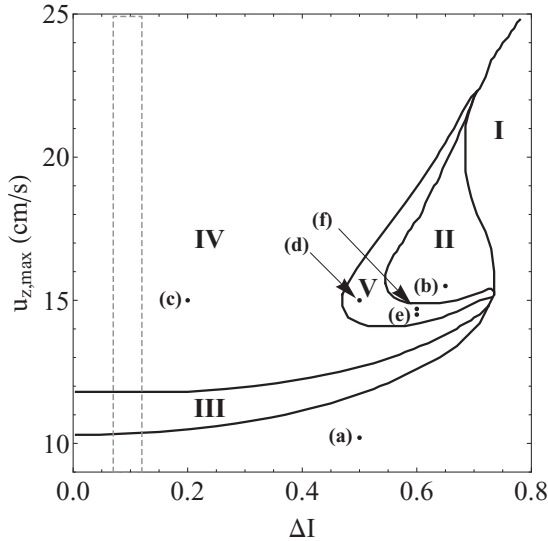


FIG. 10. The regions of the $u_{z,\max}, \Delta I$ parameter plane, characterized by different types of dynamics in the periodically time-dependent model flow. Roman numerals mark the regions, and Latin letters denote points corresponding to the parameters of the panels of Fig. 11. I, escape at the bottom (a); II, transient chaotic behavior (b); III, oscillation in the axis; IV, simple loop motion in the r - z plane (c); V, period-doubling bifurcation and permanent chaotic region (d)–(f). The “realistic” parameter domain, accessible by the experiment, lies within the dashed rectangle. Other parameters: $f = 10$ Hz, $n = 2$.

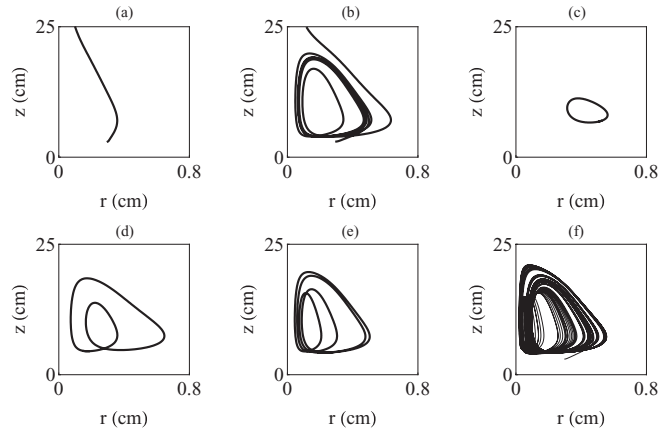


FIG. 11. Typical particle trajectories for different parameters in the r - z plane. The parameters are the same as in Fig. 10; the ΔI and $u_{z,\max}$ values corresponding to panels (a)–(f) are indicated in that figure. Initial conditions: $r_0 = 0.3$ cm, $z_0 = 3.0$ cm, and the initial velocities are 0 cm/s in all cases. In the case of (c)–(f), the first 300 s is cut off.

the particle cannot escape and goes to an attractor (periodic in III, IV, and partially chaotic in V).

On the r - z plane, we can see most often a closed curve corresponding to a periodic attractor [Figs. 11(c)–11(e)]. The most expanded area (region IV) belongs to a simple loop [Fig. 11(c)]. If we are in that region and ΔI is increasing, at the border of region IV and V the system undergoes a period-doubling bifurcation [33]. We can see that after every bifurcation, the number of loops doubles [Figs. 11(d) and 11(e)]. Within region V, permanent chaotic motion is also found [Fig. 11(f)]. The value of the Lyapunov exponent on this attractor is found to be 0.067 1/s corresponding to an e-folding time of 15 s of uncertainties. For $n > 2$, the regions become deformed, and region V becomes thinner and more insignificant.

In the experiments, irregular motion typically occurs in a much wider parameter range than in the simulation. To illustrate this, we recall from the $s(h)/h$ values of Table I that the range of ΔI is (0.07,0.12), and from measurements of [8] $u_{z,\max}$ is expected to be larger than 8 cm/s, which is plotted as a dashed rectangle in Fig. 10. Inside this region, the simulations do not exhibit any kind of irregular motion. This implies that the time-periodic model lacks an important feature of the real system.

V. TURBULENCE

A. Modeling turbulence effects

As the Reynolds number of the flow is quite high ($\approx 10^3$), it is necessary to add the effect of turbulence to the model. We do that in a relatively simple way by taking into account that turbulent vortices in the flow kick the particle and modify its velocity with a vector $\Delta \vec{v}$.

Unfortunately, we do not have any direct information or measurement on the turbulent vortices; their effect on particle motion can, however, be observed. In our simple model, we choose an exponential distribution to describe the time periods

Δt between the kicks, i.e., a Poisson process. Its probability density function, $\mathcal{F}(\Delta t)$, is thus

$$\mathcal{F}(\Delta t) = \frac{1}{\tau} \exp\left(-\frac{\Delta t}{\tau}\right), \quad (20)$$

where τ is the mean kicking time. The value $\tau = 0.01$ s appears to be an appropriate choice because this happens to be the largest value compatible with a Gaussian distribution of the velocity increments.

The direction of the vector $\Delta\vec{v}$ of velocity increments is chosen randomly in the spherical angles ϕ and θ . θ is the angle between the z axis and the direction of $\Delta\vec{v}$ ($0 < \theta < \pi$), and ϕ is the angle between the x axis and the projection of $\Delta\vec{v}$ to the xy plane ($0 < \phi < 2\pi$).

The magnitude Δv of the vector $\Delta\vec{v}$ is chosen also randomly. Its probability density function is assumed to be the Gaussian

$$P(\Delta v) = \frac{1}{\sqrt{2\pi}\sigma} \exp\left(-\frac{\Delta v^2}{2\sigma^2}\right). \quad (21)$$

Parameter σ determines the modulus of the average kick size, which should be determined later.

B. Parameter tuning

Parameters n , $u_{z,\max}$, and σ are not fixed yet. In what follows, we determine them by fitting the numerical results to the experimental data.

A first estimation of n and $u_{z,\max}$ can be obtained by comparing the periodically time-dependent simulations without kicking ($\sigma = 0$) with the measured \bar{v}_z and \bar{z} (see Table II). As Fig. 12 illustrates, the results are $n = 6$ and $u_{z,\max} = 11.9$ cm/s for $f = 10$ Hz.

The next step is to turn on kicking ($\sigma > 0$). Due to the stochastic forcing, it is not sufficient to study a single trajectory. Therefore, in what follows, an ensemble of 100 trajectories is monitored. Initially, they are distributed homogeneously in

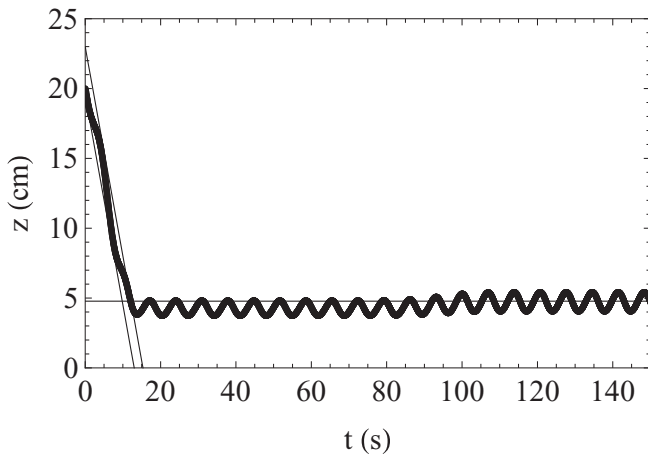


FIG. 12. Simulated vertical motion of a particle without kicking. Parameters: $f = 10$ Hz, $\Delta I = 0.07$. Initial conditions: $z_0 = 20$ cm, $r_0 = 0.01$ cm, $v = 0$ cm/s. By choosing $u_{z,\max} = 11.9$ cm/s and $n = 6$, the height of the horizontal line and the slope of the two parallel lines agree with the measured \bar{z} and \bar{v}_z (4.78 cm and 1.5 cm/s, respectively; see Table II).

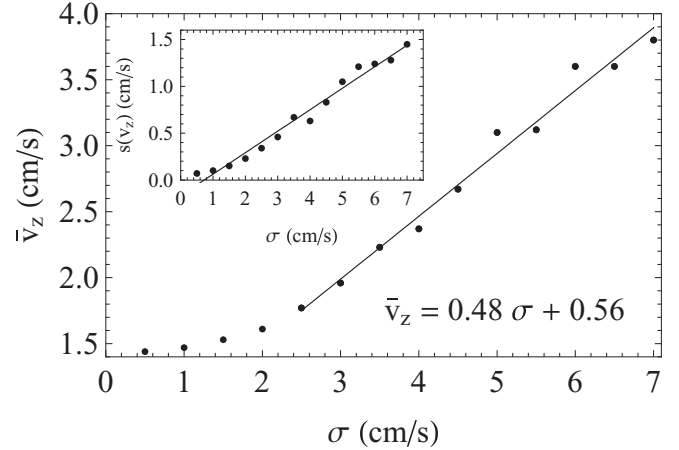


FIG. 13. Average sinking velocity \bar{v}_z of simulated particles vs the average kick size σ for $f = 10$ Hz. All other parameters are the same as in Fig. 12. Every point of the figure represents the average over 100 trajectories. The inset shows the standard deviations of the sinking velocities (compare to Table II).

the range $20 \leq z \leq 20.09$ cm, $0.001 \leq r \leq 0.01$ cm, in the $\phi = 0$ plane.

Figure 13 shows that in the presence of model turbulence, the simulated average sinking velocity \bar{v}_z depends on the average kick size σ . The reason for the effect is simple: if the particle is kicked upward, the relative velocity difference between the flow and the particle is increased, which causes a higher drag force. If the particle is kicked downward, the effect is the opposite. The net effect of the kicks is that the sinking velocity is increasing. As Fig. 13 illustrates, for $\sigma > 3$ the relation is linear. Note that the slope is relatively large (an increase of $\Delta\sigma = 1$ implies an increase of \bar{v}_z by about 0.5 cm/s, which is on the same order as the measured \bar{v}_z in Table II), indicating a strong dependence on σ . In addition, the graph depends on the value of $u_{z,\max}$, which is 11.9 cm/s in Fig. 13. Thus we conclude that a simultaneous tuning of σ and $u_{z,\max}$ is necessary even at a fixed value of n .

A rough estimation of σ is nevertheless possible based on the observation that the variance of v_z appears to be independent of $u_{z,\max}$. We emphasize that this estimation uses only the first (descending) period of the particle motion (see Fig. 3). As the inset of Fig. 13 shows, the standard deviation $s(v_z)$ of the sinking velocities obeys the linear relation

$$s(v_z) = 0.229\sigma - 0.167. \quad (22)$$

In view of the analogous experimental data of Table II for the variance of v_z (0.3, 0.4, and 0.9 cm/s), we find that $2 < \sigma < 4.6$ cm/s.

Another estimation (more established than the previous one) of σ is based on the height distribution $P(z)$. $P(z)$ in the steady state can also be deduced from the simulations. Figure 14 shows the results for $f = 10$ Hz with different σ values. A comparison of the experimental and the simulated data suggests that the best agreement is found for $\sigma \approx 5$ cm/s. The inset displays the dependence of the average lifetime \bar{T} obtained from 100 trajectories as a function of σ . Particles are considered as escaped if $z < 1$ cm. We see that for $5 \leq \sigma \leq 6$,

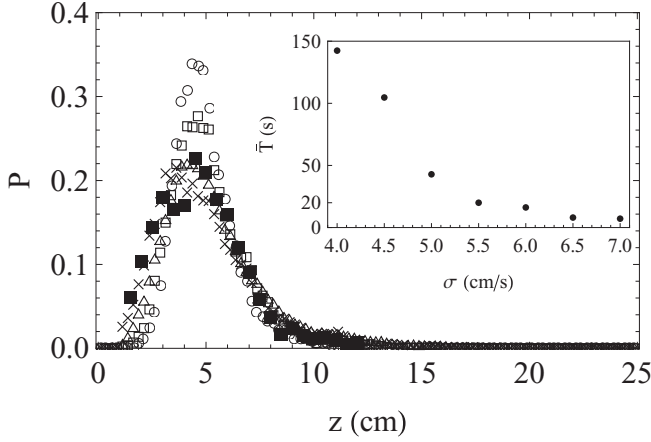


FIG. 14. Height distributions $P(z)$ for $f = 10$ Hz, $u_{z,\max} = 11.9$ cm/s, $n = 6$ with different σ values. Circle: $\sigma = 3.5$, square: $\sigma = 4.0$, triangle: $\sigma = 5.0$, and \times : $\sigma = 7.0$. The filled square marks the experimental data of the 10 Hz case. Every point of the figure represents the average over 100 trajectories. The inset displays the mean lifetime \bar{T} vs σ in the simulations.

the lifetime values are on the same order as the measured ones mentioned at the end of Sec. II B.

The third estimation of σ is based on the velocity increments that characterize instantaneous (or short time) properties of the system augmenting the previous two estimations, which are long-time properties. In Fig. 5, the histograms of the vertical component of the velocity increments are shown, and the values of σ_z are calculated from the measured signals. The same method can also be applied to calculate the analogous values (σ'_z) of the simulated trajectories where the velocity increment Δv_z is evaluated also in the simulation after $\Delta t = \tau_{\text{sample}}$. This distinction is made because we cannot be sure that it is σ'_z , which should directly correspond to the σ_z extracted from experiments. Figure 15 shows the relation between the freely chosen kick size σ and the numerically obtained average velocity increment σ'_z for $f = 10$ Hz. A direct proportionality

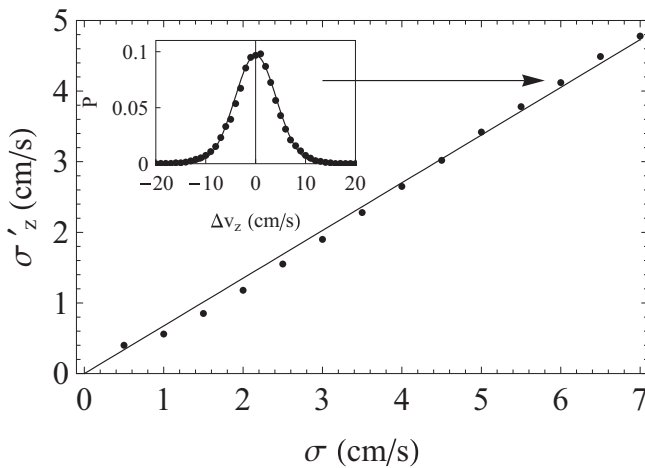


FIG. 15. Dependence of σ'_z on σ in the simulation for $f = 10$ Hz, $u_{z,\max} = 11.9$ cm/s, $n = 6$. The inset exhibits the distribution $P(\Delta v_z)$ belonging to the end point of the arrow.

TABLE IV. Correlation function values $r_1 = r(\tau_{\text{sample}})$ belonging to the sampling time and the reduction factors (see Fig. 7).

f	r_1	$\sqrt{1+r_1}$
7.5 Hz	-0.40	0.78
10.0 Hz	-0.32	0.83
12.5 Hz	-0.57	0.65
Averages	-0.43	0.75

is found,

$$\sigma'_z = 0.68\sigma. \quad (23)$$

The distributions are Gaussian for all σ , which is represented for $\sigma = 6$ cm/s by the inset. (As mentioned previously, the Gaussian property would not be true if the mean kicking time τ were significantly greater.)

Applying (23) for the estimate $\sigma = 5$ cm/s based on the height distributions, we obtain $\sigma'_z = 3.4$ cm/s. In the experiment, however, $\sigma_z = 4.6$ cm/s for $f = 10$ Hz (see Table II). The difference is considerable. It can be understood, however, by taking into account the (negative) correlations between the successive velocity increments (see Fig. 7).

To see this, let us first recall that the correlation of the velocity increments is not significant for $\Delta t \geq 2\tau_{\text{sample}}$ (see Fig. 7). Consider two successive vertical velocity increments (Δv_z) of the experiment, separated in time by τ_{sample} , as random variables ξ_1 and ξ_2 . According to our observations, both distributions are Gaussian and correlated. We denote the standard deviation for both of these variables and the coefficient of the correlation between them by σ_z and $r_1 \equiv r(\tau_{\text{sample}})$, respectively. Let us denote the random variable of the vertical velocity increments belonging to $\Delta t = 2\tau_{\text{sample}}$ by η . Naturally, $\eta = \xi_1 + \xi_2$, and if the kicks would be independent, then the standard deviation of η would be $\sqrt{2}\sigma_z$. In the correlated case, the standard deviation of η is known [34] to be $\sqrt{2(1+r_1)}\sigma_z$, which means that a correction factor $\alpha = \sqrt{1+r_1}$ appeared. For $r_1 < 0$, the factor is smaller than 1 and the correction means a reduction of the kicking compared to the uncorrelated case.

The factors $\sqrt{1+r_1}$ range between 0.65 and 0.83 (see Table IV). For simplicity, we take their average $\alpha \approx 75\%$ as a reduction factor in all three cases.

To keep our model as simple as possible, we would like to use uncorrelated kicks in (21). This can be achieved—in view of the discussion above—by interpreting the numerical results obtained with (21) as if they were obtained with kicking strength σ/α . Toward that end, we define a new quantity σ''_z ,

$$\sigma''_z = 0.68\sigma/\alpha. \quad (24)$$

This implies of course

$$\sigma''_z = \sigma'_z/\alpha. \quad (25)$$

This new quantity should be compared with the average velocity increment σ_z coming from the experiment in which anticorrelation plays an important role.

TABLE V. Parameters A' , B' , and M' of (27) used in the simulations.

f (Hz)	A'	B'	M'
7.5	-0.35	5.5	3.0
10.0	-0.25	6.1	4.4
12.5	-0.40	6.7	4.7

To summarize, by anticipating that the measured average velocity increments σ_z and σ_z'' coincide, one expects

$$\sigma = \alpha \frac{\sigma_z}{0.68} \quad (26)$$

to be a relation between the numerical realization of kicking in terms of (21) and the measured σ_z . Indeed, this formula is consistent with $\sigma \approx 5$ cm/s and $\sigma_z \approx 4.6$ cm/s.

Unfortunately, by determining the values of \bar{v}_z and \bar{z} with $\sigma \approx 5$ cm/s in a similar manner as in Fig. 12, essential differences from the measured values are found. These cannot be improved by a tuning of $u_{z,\max}$ and n either. Therefore, a consideration of a possible height dependence of σ appears to be appropriate.

C. Refined steady-state distributions

According to Fig. 6, σ_z is height-dependent. A height-dependent kicking, similar in form to (5), should be taken into account based on Fig. 6. In terms of σ , we therefore write

$$\sigma = \begin{cases} A'\bar{z} + B' & \text{if } \bar{z} \leq \frac{M'-B'}{A'}, \\ M' & \text{if } \bar{z} > \frac{M'-B'}{A'}. \end{cases} \quad (27)$$

Parameters A' , B' , M' are determined from a detailed comparison of the numerically determined $\sigma_z''(\bar{z})$, based on relation (25) and the experimental $\sigma_z(\bar{z})$ functions. The best fit of the parameters found from the simulations are given in Table V. The insets of Figs. 16–18 illustrate the degree of agreement.

After these steps, parameters n and $u_{z,\max}$ can be chosen by the requirement of an agreement as good as possible between the simulated and measured \bar{v}_z and \bar{z} values. This is based on the property that an increase of $u_{z,\max}$ and n leads to an

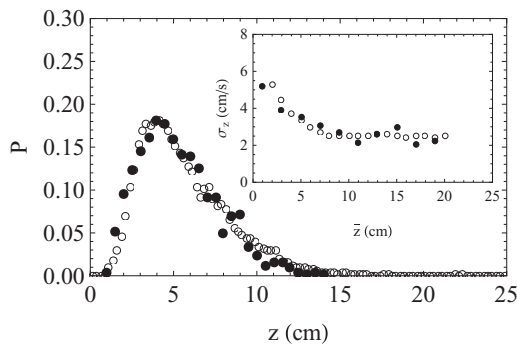


FIG. 16. The measured (filled circles) and the numerically calculated (circle) height distribution for $f = 7.5$ Hz. Parameters: $\Delta I = 0.09$, $n = 9$, and $u_{z,\max} = 11.1$ cm/s. Inset: dependence of the average velocity increment on height [measurement, σ_z : filled circle; simulation, σ_z'' (24): circle].

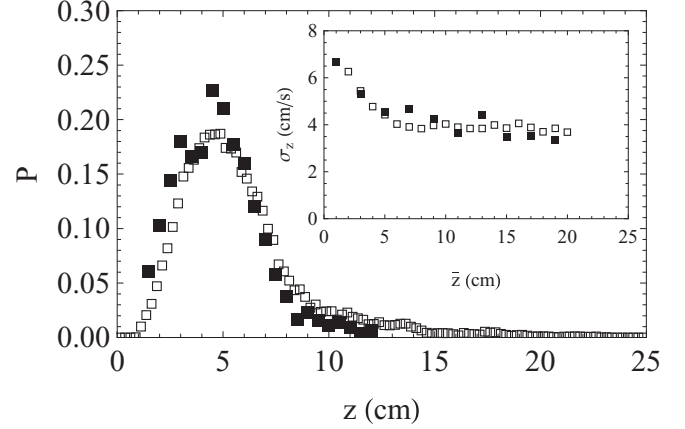


FIG. 17. The measured (filled squares) and the numerically calculated (squares) height distributions for $f = 10$ Hz. Parameters: $\Delta I = 0.07$, $n = 7$, and $u_{z,\max} = 10.8$ cm/s. Inset: dependence of the average velocity increment on height [measurement, σ_z : filled squares; simulation, σ_z'' (24): squares].

increase of \bar{v}_z and a decrease of \bar{z} , respectively. The results are summarized in Table VI. Note that the fitted values of exponent n in (7) turn out to be rather large, corresponding to a nearly constant g function at midheights.

At the end, the measured and the numerically calculated height distributions can be compared as shown by Figs. 16–18. The agreements are good considering the simplicity of the model.

At this point the following question naturally arises: Which parameters and features of our model have the most important contribution to the right description of the experimental results? According to the simulations, if ΔI is smaller than the used values, the distributions do not change essentially. Toward the higher values of ΔI , however, the distributions flatten and broaden. It can also be found that the effect of the fluid oscillation is so weak compared to the kicks (model

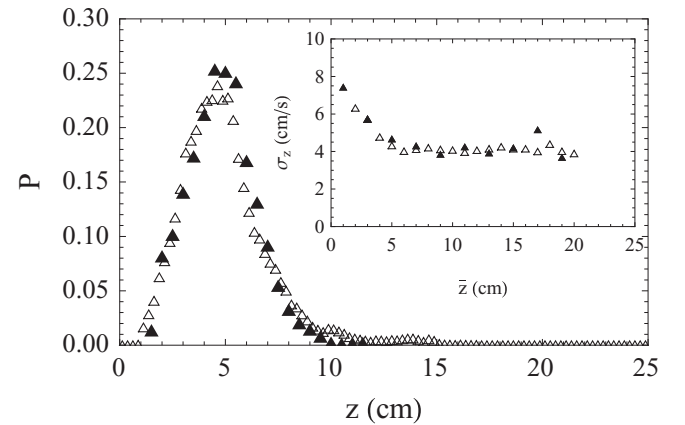


FIG. 18. The measured (filled triangles) and the numerically calculated (triangles) height distributions for $f = 12.5$ Hz. Parameters: $\Delta I = 0.07$, $n = 7$, and $u_{z,\max} = 11.1$ cm/s. Inset: dependence of the average velocity increment on height [measurement, σ_z : filled triangles; simulation, σ_z'' (24): triangles].

TABLE VI. The statistical properties of the simulated particle dynamics (\bar{v}_z and \bar{z} values) with the best fit of $u_{z,\max}$ and n for the different frequencies f (compare with Table II).

f (Hz)	\bar{v}_z (cm/s)	\bar{z} (cm)	$u_{z,\max}$ (cm/s)	n
7.5	1.15	5.68	11.1	9
10.0	1.73	4.72	10.8	7
12.5	2.08	5.03	11.1	7

turbulence) that it cannot cause any measurable correlation in the motion of the particle.

If the kicks are height-independent, the kicks at the bottom turn out to be weaker than realistic. This increases the particle's lifetimes; moreover, in some cases it even makes the escape at the bottom impossible. This is in clear contrast with the observations described in Sec. II. In other words, the height dependence is essential for the correct escape dynamics. Without this, the distribution differs markedly from the measured one, and the typical region where the particle moves appears to be broader.

On the other hand, the kick reduction, albeit not enormous (75%), seems to play a crucial role: without it, the particle escapes too fast (i.e., the lifetimes are too short) and the correct determination of the distribution becomes difficult, since the particle practically just runs through the studied domain.

VI. SUMMARY AND CONCLUSION

In this paper, we studied the motion of an inertial buoyant particle in a time-dependent three-dimensional vortex. We have constructed a series of models of increasing complexity to provide an acceptable minimal model for the experimentally observed dynamics. At each stage, new features have been introduced, as follows: (i) motion of an inertial particle in a time-independent vortex, (ii) periodic time dependence of the flow, (iii) model turbulence (simple kicks with height independent σ), (iv) reduction caused by the anticorrelated successive velocity increments, and (v) height dependence of the strength of kicks. The role of stage (i) is to describe roughly the first, descending part of the particle motion (see Fig. 3). (ii) opens up the possibility for the appearance of chaos. However, the parameter domain where chaos exists in the simulations and in the experiments is disjoint (see Fig. 10). This observation led us to the conclusion that the reason for the observed zigzag motion of the particle cannot be explained solely by the periodic time dependence of the background flow. Therefore, stage (iii) was necessary to capture the properties of the real particle motion, and finally, both (iv) and (v) proved necessary to reproduce the measured data quantitatively.

It is worth noting that the last levels lead to a drastic change in the character of the particle dynamics. On the time scale of a few seconds, a roughly exponential separation of nearby particles can be observed, but much faster than in the chaotic cases without kicking. Carrying out a similar estimation to that in Sec. IV B for Fig. 11(h), the analog of a Lyapunov exponent is obtained to be about 1 1/s, more than ten times larger than originally. In addition, this order of magnitude

is also characteristic of cases that are nonchaotic without kicking. We thus conclude that noise plays a dominant role in the dynamics, i.e., the chaoticity of the particle motion is not of low-dimensional origin. It is instead a consequence of the interaction with a many-degree-of-freedom environment, representing local small-scale turbulence in the flow.

ACKNOWLEDGMENTS

This research was supported by OTKA Grant No. NK100296. Support from the Alexander von Humboldt Foundation is acknowledged. We thank E. Á. Horvát for her contributions in a preliminary stage of this study, and A. Daitche for helpful remarks.

APPENDIX: NUMERICAL DETERMINATION OF THE FUNNEL

By means of the Navier-Stokes equations, it is possible to calculate the function $h(r)$ describing the shape of the free surface (funnel) in a steady flow. The local water height at distance r is then $z(r) = H_w - h(r)$, where H_w is the ambient water height. To obtain the function $h(r)$, we need to determine the isobaric surfaces. Because of the symmetry, we use cylindrical coordinates. Along an isobar,

$$dp(r, z) = 0, \quad (\text{A1})$$

that is,

$$\frac{\partial p}{\partial r} dr + \frac{\partial p}{\partial z} dz = 0. \quad (\text{A2})$$

Therefore,

$$\frac{dz}{dr} = -\frac{dh}{dr} = -\frac{\partial p}{\partial r} / \frac{\partial p}{\partial z}. \quad (\text{A3})$$

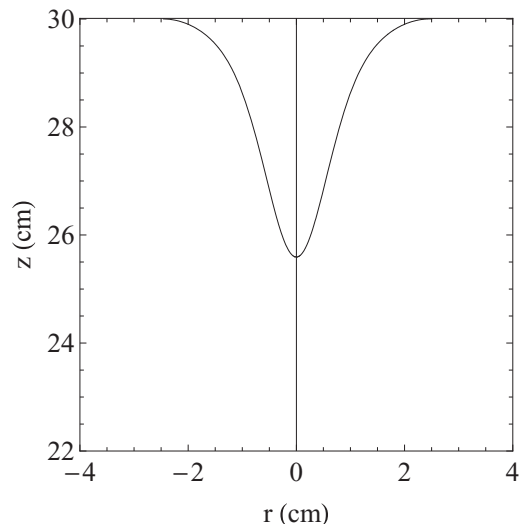


FIG. 19. The numerically calculated free surface $z(r) = H_w - h(r)$ in a steady flow. Parameters: $H_w = 30$ cm, $f = 10$ Hz ($n = 7$ and $u_{z,\max} = 10.8$ cm/s). The funnel height is found to be $h = 4.4$ cm.

From here,

$$h(r') = \int_0^{r'} \frac{\partial p}{\partial r} / \frac{\partial p}{\partial z} dr, \quad (\text{A4})$$

where the partial derivatives in the integrand can be expressed from the radial and z components of the cylindrical form of the Navier-Stokes equations. These partial derivatives are [29]

$$\begin{aligned} \frac{\partial p}{\partial r} = \rho \left[-u_r \frac{\partial u_r}{\partial r} - u_z \frac{\partial u_r}{\partial z} + \frac{u_\phi^2}{r} \right. \\ \left. + \nu \left(\frac{1}{r} \frac{\partial u_r}{\partial r} + \frac{\partial^2 u_r}{\partial r^2} + \frac{\partial^2 u_r}{\partial z^2} - \frac{u_r}{r^2} \right) \right] \quad (\text{A5}) \end{aligned}$$

and

$$\begin{aligned} \frac{\partial p}{\partial z} = \rho \left[-u_r \frac{\partial u_z}{\partial r} - u_z \frac{\partial u_z}{\partial z} \right. \\ \left. + \nu \left(\frac{1}{r} \frac{\partial u_z}{\partial r} + \frac{\partial^2 u_z}{\partial r^2} + \frac{\partial^2 u_z}{\partial z^2} \right) + g \right]. \quad (\text{A6}) \end{aligned}$$

Substituting this into (A4), the shape $h(r)$ of the funnel can be obtained numerically. Toward that end, parameter H in (7) is replaced by the full water height H_w , and all the relations (8)–(13) are kept to determine the flow field. An example of the funnel's shape with $H_w = 30$ cm is provided by Fig. 19. The funnel height h (and the water height H below the funnel) is obtained as $h = h(0)$ [and $H = H_w - h$ (see Fig. 1)]. The result of Fig. 19 illustrates that the choice $H = 25$ cm used throughout the paper is a good approximation.

-
- [1] J. Magnaudet and I. Eames, *Annu. Rev. Fluid Mech.* **32**, 659 (2000).
- [2] R. O. Medrano-T, A. Moura, T. Tél, I. L. Caldas, and C. Grebogi, *Phys. Rev. E* **78**, 056206 (2008).
- [3] F. Toschi and E. Bodenschatz, *Annu. Rev. Fluid Mech.* **41**, 375 (2009).
- [4] J. H. E. Cartwright, U. Feudel, G. Károlyi, A. de Moura, O. Piro, and T. Tél, in *Nonlinear Dynamics and Chaos: Advances and Perspectives*, edited by M. Thiel *et al.* (Springer, New York, 2010), p. 51.
- [5] G. Metcalfe, M. F. M. Speetjens, D. R. Lester, and H. J. H. Clercx, *Adv. Appl. Mech.* **45**, 109 (2012).
- [6] R. Toegel, S. Luther, and D. Lohse, *Phys. Rev. Lett.* **96**, 114301 (2006).
- [7] V. Garbin *et al.*, *Phys. Fluids* **21**, 092003 (2009).
- [8] G. Halász, B. Gyüre, I. M. Jánosi, K. G. Szabó, and T. Tél, *Am. J. Phys.* **75**, 1092 (2007).
- [9] L. Giannelli, A. Scoma, and G. Torzillo, *Biotech. Bioeng.* **104**, 76 (2009).
- [10] N. Petit, J. Ignes-Mullol, J. Claret, and F. Sagues, *Phys. Rev. Lett.* **103**, 237802 (2009).
- [11] L. L. Lazarus *et al.*, *ACS Appl. Mater. Interfaces* **4**, 3077 (2012).
- [12] G. Huang *et al.*, *Talanta* **100**, 64 (2012).
- [13] H. Rezvantab and S. Shojaei-Zadeh, *J. Coll. Interface Sci.* **400**, 70 (2013).
- [14] S. Shakerin, *Phys. Teach.* **48**, 316 (2010).
- [15] U. Frisch, *Turbulence* (Cambridge University Press, Cambridge, 1995).
- [16] N. Mordant *et al.*, *J. Stat. Phys.* **113**, 701 (2003).
- [17] Y. X. Huang *et al.*, *Europhys. Lett.* **86**, 40010 (2009).
- [18] J. C. Vassilicos and J. C. H. Fung, *Phys. Fluids* **7**, 1970 (1995).
- [19] J. C. H. Fung, *J. Aerosol Sci.* **28**, 753 (1997).
- [20] J.-R. Angilella, *Phys. Fluids* **19**, 073302 (2007).
- [21] M. R. Maxey and J. J. Riley, *Phys. Fluids* **26**, 883 (1983).
- [22] T. R. Auton, J. C. R. Hunt, and M. Prud'homme, *J. Fluid Mech.* **197**, 241 (1988).
- [23] R. Mei and R. J. Adrian, *J. Fluid Mech.* **237**, 323 (1992).
- [24] R. Mei, *J. Fluid Mech.* **270**, 133 (1994).
- [25] W. C. Park, J. F. Klausner, and R. Mei, *Exp. Fluids* **19**, 167 (1995).
- [26] E. Loth and A. J. Dorgan, *Environ. Fluid Mech.* **9**, 187 (2009).
- [27] E. E. Michaelides, *J. Fluid Eng.* **119**, 233 (1997).
- [28] A. Daitche and T. Tél, *Phys. Rev. Lett.* **107**, 244501 (2011).
- [29] P. K. Kundu and I. M. Cohen, *Fluid Mechanics* (Academic, San Diego, 1990).
- [30] F. M. White, *Viscous Fluid Flow*, 2nd ed. (McGraw-Hill, New York, 1991), p. 182.
- [31] E. Calzavarini *et al.*, *Physica D* **241**, 237 (2012).
- [32] Y. C. Lai and T. Tél, *Transient Chaos* (Springer, Berlin, 2011).
- [33] E. Ott, *Chaos in Dynamical Systems* (Cambridge University Press, Cambridge, 1993).
- [34] A. Papoulis, *Probability, Random Variables and Stochastic Processes*, 3rd ed. (McGraw-Hill, New York, 1991), p. 155.